NJC

PAPER

View Article Online
View Journal | View Issue

Check for updates

Cite this: *New J. Chem.*, 2018, **42**, 6763

Received 12th December 2017,
Accepted 19th March 2018

DOI: 10.1039/c7nj04922f

rsc.li/njc

# Preparation of porous carbon electrodes from semen cassiae for high-performance electric double-layer capacitors†

Ji-Shi Wei,[a] Suige Wan,[b] Peng Zhang,[a] Hui Ding,[c] Xiao-Bo Chen,[d]
Huan-Ming Xiong,*[a] Shuyan Gao[b] and Xianjun Wei*[b]

A series of sponge-like hierarchical porous carbons are prepared using semen cassiae as the precursor and potassium oxalate monohydrate as the activation agent. These sponge-like carbon materials have high surface areas, wide distributions of pore size, and the appropriate forms of nitrogen/oxygen derivatives. All these advantages in structures and surface states contribute to the outstanding performances of such materials as electrodes for high performance electric double-layer capacitors, which include high specific capacitance, high cycling stability, and high energy density. For example, the optimal sample exhibits a high specific capacitance of 401 F $g^{-1}$, excellent cycling stability (94.5% retention after 10 000 cycles), high energy density (12.01 W h $kg^{-1}$) and a high power density (10 200 W $kg^{-1}$) in 1 M $H_2SO_4$ solution.

## Introduction

Electric double-layer capacitors (EDLCs), a key category of energy-storage devices with a long lifespan and superior power density, are essentially required for high-performance fuel cells, solar cells and power batteries.[1] Nevertheless, in comparison with those for batteries, EDLCs always exhibit low energy density or specific capacitance, and thus unsatisfactory performance, which limits their use in practical applications.[2] Based on their working principles, namely ions adsorption/desorption on electrode surface, the electric conductivity, surface area, pore size distribution and surface states regulate the electrochemical performance of EDLCs to a great magnitude. The electric conductivity, surface area, pore size distribution and surface states regulate the electrochemical performance of EDLCs to a great extent.[1] Accordingly, metal oxide or conductive polymer based materials with diverse morphologies and structures have been prepared. For bare $RuO_2$ or sole polyaniline,[3,4] although they exhibit high energy density with sacrificed power density, their low rate capability remains a technical issue. On the other hand, hierarchical porous carbon derived from polymer precursors,[5] graphene with a super large specific surface area (more than 3000 $m^2$ $g^{-1}$),[6] and 3D meso-pore carbon with a uniform pore size have all been developed as EDLC type electrode materials.[7] Large specific capacitance (more than 300 F $g^{-1}$) and a high capability rate (more than 60%) make the carbon based materials a promising material of choice.

Unfortunately, most of those carbon materials suffer from either uncommon precursors or complex synthetic processes, thus hindering their upscale employment. As such, cost-effective carbon materials with simple preparation techniques is of great significance for the commercialization of EDLCs.[8] Biomass just is a cost-effective and environmentally-benign supplier for generating carbon electrode materials with high electric conductivity, large surface area and abundant surface functional groups.[9,10] In addition, reuse of massive discarded biological resources is of great importance for a sustainable environment and economy. Therefore, biomass based carbon electrodes will be a feasible option for high-performance EDLCs with a number of benefits. First, many natural biomaterials have unique and periodic structures.[2] Of these, the crab shell which exhibits an uniform porous structure can be used as a hard template to prepare ordered mesoporous carbon nanofibers.[11] Second, carbon materials could match well with the appropriate electrolytes and their performances would be greatly improved through delicate controls over the surface area and pore size.[5] Third, heteroelements, such as N, P, S, *etc.* as the original ingredients of biomass, will be involved in the biomass-made carbon electrodes and contribute greatly to the pseudocapacitance, electron transport and surficial wettability.[8] In addition, special interest should

---

[a] *Department of Chemistry and Shanghai Key Laboratory of Molecular Catalysis and Innovative Materials, Fudan University, Shanghai 200433, P. R. China. E-mail: hmxiong@fudan.edu.cn*

[b] *Key Laboratory of Green Chemical Media and Reactions (Ministry of Education) and School of Chemistry and Chemical Engineering, Henan Normal University, Xinxiang Henan 453007, P. R. China. E-mail: xj_wei@163.com*

[c] *College of Chemical Engineering, China University of Mining and Technology, Xuzhou Jiangsu 221008, P. R. China*

[d] *School of Engineering, RMIT University, Carlton, VIC 3053, Australia*

† Electronic supplementary information (ESI) available. See DOI: 10.1039/c7nj04922f

be cast onto the selection of the appropriate activation agents to promote the yield quality of the calcination process. Biomass based carbon materials are often obtained through pyrolysis with the aid of physical or chemical additives for activation, which can enlarge the active surface area and introduce a porous structure eventually.[8,12] As a result, a sound calcination treatment and the selection of the appropriate activation agents are also of great importance. Typically, in the activation process, some chemicals such as potassium hydroxide (KOH) and zinc chloride ($ZnCl_2$) are able to increase the surface area effectively even under an inert atmosphere. However, such violent chemical reactions contain several issues, such as a low yield rate (usually no more than 25%), severe environmental pollution and equipment degradation incurred by the activation agents.[12] Thus, the appropriate activation agent would make one-step carbonization more cost-effective, environmentally friendly and safe.

Semen cassiae (SC), seeds of an annual plant – Sicklepod (*Cassia obtusifolia*) which is widely cultivated in China, is commonly used as a traditional herbal medicine and roasted tea. All cassia plant parts contain fatty acids, amino acids, phenolic compounds, flavonoids and proanthocyanidins,[13,14] which will supply abundant functional groups for faradic reactions, like carboxyl, hydroxyl, *etc.* After calcination, SC has both a high carbon content and low ash content so as to provide a solid carbon skeleton structure for high performance EDLCs. Meanwhile, potassium oxalate ($K_2C_2O_4$) was selected as a mild activation agent, contributing to the preparation of porous carbon with a large surface area, hierarchical structure and abundant surficial functional groups through a facile way. During this process, $K_2C_2O_4$ will gradually decompose into $K_2CO_3$, $K_2O$, CO and $CO_2$ as the carbonization temperature rises. The resulting $K_2O$ and $CO_2$ will further react with carbon, which makes the carbon skeleton become thinner and facilitates the formation of a porous structure.[15,16] And this process is relatively slow in comparison with the typical activation by KOH or $ZnCl_2$. Therefore, such a mild process does not need pre-carbonization and the final yields can be over 60%. The optimal sample exhibits a high specific capacitance of 401 F $g^{-1}$, excellent cycling stability (94.5% retention after 10 000 cycles), high energy density (12.01 W h $kg^{-1}$) and a high power density (10 200 W $kg^{-1}$) in 1 M $H_2SO_4$ solution. Overall, such a kind of green and cost-effective biomass and the appropriate activation agent would provide new insights for the design and preparation of carbon based electrodes for high-performance EDLCs for a great variety of energy related applications.

## Experimental

### Materials

Seeds of semen cassiae (SC) were harvested in Ningxia, China. Potassium oxalate monohydrate ($K_2C_2O_4{\cdot}H_2O$), sulfuric acid ($H_2SO_4$), hydrochloric acid (HCl), ethanol, and other chemicals were purchased from Shanghai Chemical Corp. All chemicals were used as received.

### Preparation of sponge like porous carbon

The seeds were dried in vacuum at 60 °C for 24 h. Then, they were mixed with a $K_2C_2O_4$ aqueous solution (40 wt%) by a mass ratio of 1 : 3 (optimized condition) for 12 h. Afterwards, the mixture was dried in vacuum at 80 °C for 12 h. The impregnated materials were heated to 600, 700, and 800 °C at a rate of 5 °C $min^{-1}$ in a tube furnace, and then maintained at the desired temperature for 2 h. The entire process was under a nitrogen atmosphere with a flow rate of 80–100 mL $min^{-1}$. The products were washed with 1 M HCl solution to remove inorganic salts and then with distilled water and ethanol repeatedly. Finally, the products were dried in a vacuum oven at 80 °C for 24 h. The products were loose and porous carbon materials with a yield of about 60–70%.

### Characterizations

X-ray diffraction (XRD) patterns at Bragg's angle ($2\theta$) ranging from 10–90° were collected at room temperature using a Bruker D4 Endeavor X-ray diffractometer with Cu Kα radiation ($\lambda$ = 0.1541 nm, 40 kV). Fourier transform infrared (FTIR) spectra were recorded on a PerkinElmer Avatar 360 ESP FTIR spectrometer over a range of 4000–400 $cm^{-1}$, using the KBr pellet method. Nitrogen adsorption–desorption measurements were performed at 77.3 K with a Quantachrome Autosorb SI surface area analyzer to obtain the specific surface area (SSA), total pore volume, pore size distribution (PSD), *etc.* X-ray photoelectron spectroscopy (XPS) data were obtained with a Thermo ESCALAB 250 electron spectrometer using an Al Kα X-ray source (1486.6 eV). Morphologies of the samples were characterized through scanning electron microscopy (SEM, JSM-6390) and high-resolution transmission electron microscopy (JEM-2010) at 200 kV.

### Electrochemical measurements

All electrochemical tests were conducted with a CH Instruments 660E electrochemical workstation and a CT2001A Land cell tester in 1 M of aqueous $H_2SO_4$ electrolyte with three-electrode or two-electrode cell systems. A stainless steel grid with an activated carbon film, which was prepared by pressing a mixture of the prepared carbon or commercial activated carbon (80 wt%), acetylene black (10 wt%), and a polytetrafluoroethylene binder (10 wt%) onto a stainless steel grid with an area of 1 and 3 $cm^2$ (1.5 mg $cm^{-2}$), served as the working and counter electrodes, respectively. $Hg/Hg_2SO_4$ (in saturated $K_2SO_4$ solution) served as the reference electrode. Galvanostatic charge–discharge (GCD) tests were performed over a potential range of −0.8 to 0.2 V, while the current density was varied from 1 to 30 A $g^{-1}$. Frequency limits of electrochemical impedance spectroscopy (EIS) measurements were set at 100 kHz–0.01 Hz with 5 mV of voltage amplitude at open-circuit potential. Symmetric EDLCs were assembled by using the optimal sample as the positive electrode and negative electrode, and 1 mol of $H_2SO_4$ solution as electrolyte. Cyclic voltammetry (CV) and GCD tests of the assembled EDLCs were performed on a CH Instruments 660E electrochemical workstation and a CT2001A Land cell tester. CV tests were recorded over a potential range of 0–1 V and the scan rate was set from 2 to 100 mV $s^{-1}$. GCD tests were also performed over the potential range of 0–1 V, while the current density varied from 1 to 30 A $g^{-1}$.

For the three-electrode system, $C_m$ is the gravimetric-specific capacitance of the single electrode (working electrode, F $g^{-1}$).

$$C_m = I \times t/(m \times \Delta V) \tag{1}$$

where $C_m$ is the specific capacitance, $I$ is the current, $t$ is the discharge time, $m$ is the mass of the active material of a single electrode, and $\Delta V$ is the discharge voltage.

For symmetric capacitors, gravimetric-specific capacitance ($C_m$, F g$^{-1}$), energy density ($E$) and power density ($P$) of capacitor are calculated according to the following equations:

$$C_m\ (\mathrm{F\ g^{-1}}) = I \times \Delta t/(M \times \Delta U) \tag{2}$$

$$E = 0.5 \times C_m \times \Delta U^2 \tag{3}$$

$$P = E/\Delta t \tag{4}$$

where $I$ is the constant current applied, $\Delta t$ is the discharge time, $\Delta U$ is the operating voltage of the symmetric capacitor (1.0 V), $M$ is the total weight of positive and negative materials (for symmetric capacitors, $M = 2 \times m$).

## Results and discussion

Scheme 1 illustrates the preparation process of the activated semen cassiae (ASC) carbon materials. These products are denoted as ASC-600, ASC-700 (optimal sample) and ASC-800, where the numbers represent the carbonization temperature. For further comparison, seeds were also calcined at 700 °C without adding $K_2C_2O_4{\cdot}H_2O$ (designated as SC-700) as controls.

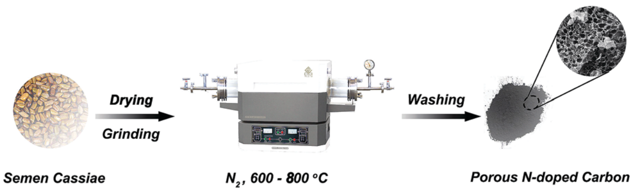

Scheme 1 Synthetic illustration of the preparation of porous carbon from SC.

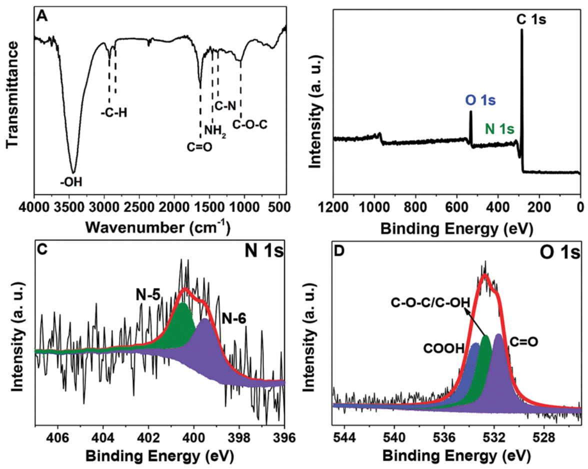

Fig. 1 (A) FTIR spectra, (B) XPS survey spectra, and high-resolution XPS of (C) N 1s and (D) O 1s of ASC-700.

The compositions and structures of ASC-700 are characterized by FTIR, XPS, Raman spectroscopy, XRD, adsorption/desorption measurements, PSD analysis and electronic microscopy (Fig. 1–3), respectively. Semen cassia with complex components, like amino acids, fatty acids and so on (molecular formulae of the main components in semen cassia are shown in Fig. S1, ESI†). Therefore, carbon materials based on SC are composed of various element forms. FTIR spectra (Fig. 1A and Fig. S1A, ESI†) reveal that four bands at 3450, 1690, 1450 cm$^{-1}$, 1380 correspond to the –OH, C=O, –NH$_2$ and C–N stretching vibrations, respectively.[5] Another broad band within 1000–1200 cm$^{-1}$ contains the stretching vibrations of C–O–C (*ca.* 1040 cm$^{-1}$).[5] XPS was employed to study the elemental composition of the ASC-700 surface. The broad XPS survey (Fig. 1B) confirms the presence of carbon, nitrogen, and oxygen in ASC-700, whilst no potassium residues are evident. In Fig. 1C, the N 1s spectra can be deconvoluted into two peaks corresponding to N-6 (pyridine type nitrogen; BE = 399.5 eV) and N-5 (pyrrolic nitrogen; BE = 400.5 eV), respectively.[17–19] The O 1s spectra (Fig. 1D) can be deconvoluted into three different species. They are C=O groups or quinone (BE = 531.7 eV), –OH and/or C–O–C groups (BE = 532.6 eV) and COOH carboxyl groups (BE = 533.6 eV).[20,21] The XPS information of all three samples is summarized in Fig. S1B and Table S1 (ESI†). It can be noted that the nitrogen of the activated carbon materials (ASC-600 and ASC-700) exhibits two chemical forms, namely N-6 and N-5, which contribute greatly to the pseudocapacitance and surficial wettability of the yielded electrode materials.[5] In contrast, the oxygen-based functional groups can also enhance pseudocapacitance, though the excess oxygen-based functional groups impose a negative impact on the ion migration rate and electrical conductance.[5] According to previous studies by our group and other scientists, the redox reactions of these nitrogen/oxygen derivatives are considered as follows.[5]

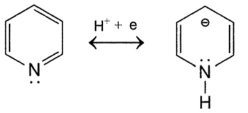

(Reaction 1)

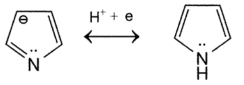

(Reaction 2)

$$\sim\mathrm{C\text{-}OH} \xleftrightarrow{\mathrm{H^+ + e}} \sim\mathrm{C=O} \xleftrightarrow{\mathrm{H_2O, H^+ + e}} \sim\mathrm{COOH}$$ (Reaction R3)

As in the above Faraday processes, such a reversible reaction is able to enhance the electrode capacitance. Data in Table S1 (ESI†) suggest that the activation agent and calcination temperature have a slight influence on the content of surface oxygen based groups. This demonstrates $K_2C_2O_4$ is a mild activation agent, therefore, it can minimize the change of the entire element distribution and mitigate the corrosive attack onto the related preparation equipment. From this viewpoint, $K_2C_2O_4$ has obvious advantages than KOH, $ZnCl_2$ and some other competitive activation agents.[22,23]

The Raman spectra in Fig. 2A and Fig. S2A (ESI†) display three absorbance regions: the D-band near 1350 cm$^{-1}$ (C–C, disordered graphite structure), the G-band near 1590 cm$^{-1}$ (sp$^2$-hybridized carbon) and the 2D-band near 2770 cm$^{-1}$.[5,16] Of these, the 2D-band is incurred by the double resonant Raman scattering with two-phonon emissions and it can reflect layer carbon to some extent. In this study, the 2D-bands of all

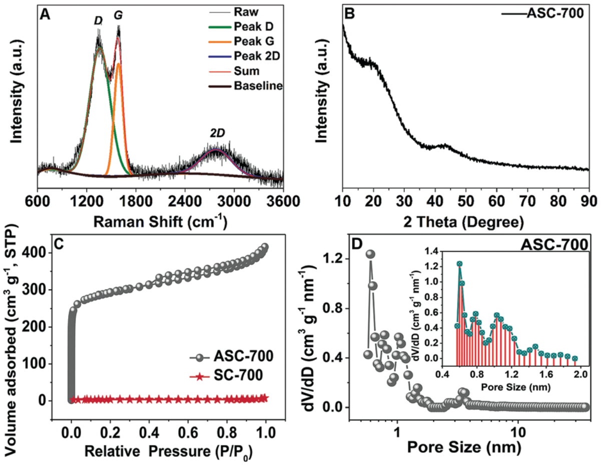

Fig. 2 (A) Raman spectra, (B) XRD pattern, (C) nitrogen adsorption–desorption isotherms, and (D) PSD calculated by the DFT method of ASC-700.

samples belong to broad peaks and their intensity is much lower than the corresponding G-band, which suggests the multi layer structures of these carbon materials. The intensity ratio of $I_D/I_G$, which represents the relationship between disorderly carbon and orderly graphitized carbon, increases from 1.08 to 1.16 with the increase in activation temperature, indicating an increasing disorder degree. This phenomenon has even been reported in our previous publication.[24] In comparison, the intensity ratio of SC-700 approaches 0.92, signifying that the activation reactions generated by $K_2C_2O_4$ will destroy the graphitized structure to a certain extent.[5,24] XRD patterns of ASC-700 and other samples are shown in Fig. 2B and Fig. S2B (ESI†), respectively, which consist of two broad diffraction peaks with $2\theta$ values of about 23.5°, and 43.5° corresponding to the (002) and (101) planes of graphitic carbon materials, respectively.[5] It is evident that the half-peak width of SC-700 is smaller than those of the other counterparts, confirming that SC-700 has a higher ordered degree in terms of graphite structure, which is consist with the results of Raman spectra.

Surface areas and porous features of the samples are evaluated by nitrogen physisorption measurements at 77.3 K (Fig. 2C, D, Fig. S3 (ESI†) and Table 1, Table S2 (ESI†)). The nitrogen adsorption isotherm curves for ASC-700 and other activated carbons exhibit a mixture of both type I and type IV characteristics, and the presence of distinct H4-type hysteresis loops at relative pressures of 0.4–1.0, which indicate that these systems contain slit-like micro/mesopores and the micropores are dominant.[5] The PSD obtained from DFT calculations demonstrates that these materials have hierarchical porous structures assembled by micropores and mesopores. However, sample SC-700 shows a much smaller SSA (specific surface area, 10.2 $m^2 g^{-1}$) and pore volume (0.02 $cm^3 g^{-1}$) than the activated samples. Besides, its pore sizes also present a narrow distribution of mesopores. Hence, the activation agent $K_2C_2O_4$ has an extraordinary impact on both the SSA and PSD of the carbon materials. Comparing ASC-700 with other two samples (ASC-600 and ASC-800), the optimal sample has a diverse distribution of pore sizes which effectively promotes both the ion storage by micropores and the ion transportation through mesopores. In addition, both the specific area and the total pore volume of ASC-700 are the largest among those data of the three activated carbons, which provides the highest site density for ion adsorption. At low carbonization temperatures (like 600 °C), $K_2C_2O_4$ will decompose into $K_2CO_3$ and CO. The released CO could assist in the removal of pyrolysis volatiles to enhance the activation degree and develop the porous carbon framework.[15] Such an activation will reach a higher degree at 700 °C as $K_2CO_3$ decomposes into $CO_2$. But when the temperature increases up to 800 °C, the walls of some micropores collapse to form micropores, resulting in the decreased specific surface areas and total volumes of ASC-800. Therefore, ASC-700 has the most developed porous structure and the largest specific surface area among all samples (Table 1). These phenomena are very similar to those reported in the literatures.[25,26] Therefore, the activation agent and calcination temperature play a synergistic role in determining the SSA, PSD, pore volume and the pore type of carbons. Regarding $K_2C_2O_4$, it acts simultaneously as the dehydration reagent and the template during the calcination process and regulate the porosity of the carbon skeletons.[27]

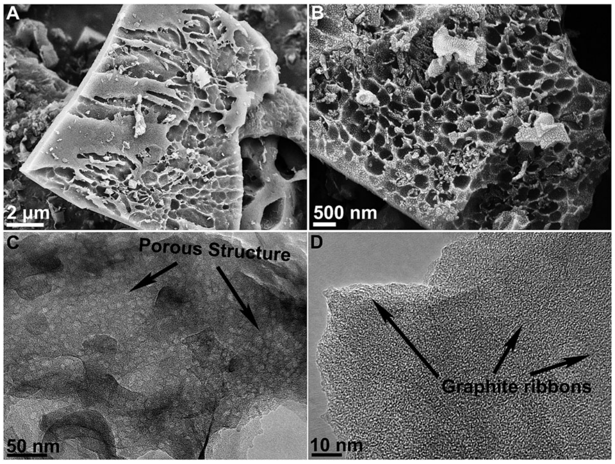

Fig. 3 (A and B) SEM and (C and D) TEM micrographs of ASC-700.

Microstructures of ASC-600, 700 and 800 are examined by SEM and TEM. Representative SEM micrographs taken at varying magnifications are shown in Fig. 3A, B and Fig. S4 (ESI†). It is evident that the activation agent could effectively introduce porous structures to carbon materials. In addition, as the calcination temperature increases, the layers of carbon become thinner and the pores of the surface increase first and then decrease. The same phenomenon is indicated in the TEM images (Fig. 3C, D and Fig. S5, ESI†). When a lower calcination temperature is

Table 1 Porosity properties of different samples

| Sample | $S_{BET}$ ($m^2 g^{-1}$) | $S_{micro}$ ($m^2 g^{-1}$) | $V_{tot}$ ($cm^3 g^{-1}$) | $V_{micro}$ ($cm^3 g^{-1}$) | $S_{micro}/S_{BET}$ | $V_{micro}/V_{meso}$ |
|---|---|---|---|---|---|---|
| ASC-600 | 655.4 | 440.1 | 0.46 | 0.18 | 0.67 | 0.64 |
| ASC-700 | 1123.8 | 907.4 | 0.64 | 0.36 | 0.81 | 1.29 |
| ASC-800 | 1060.5 | 1006.0 | 0.53 | 0.38 | 0.95 | 2.53 |
| SC-700 | 10.2 | — | 0.02 | — | — | — |

employed (*i.e.* 600 °C), the number of activated reaction sites is small, leading to a few number of pores. As the temperature goes up, the activation capacity of the activator will be enhanced. When the temperature is up to 700 °C, carbon materials with sufficiently developed pore structures are obtained. Nevertheless, excess heat (*i.e.* 800 °C) produces a series of vigorous activation reactions, which may destroy the original structure. In other words, the activating regent will not work at full capacity at low temperature (600 °C). Meanwhile, the partial porous structure will collapse at high temperature (800 °C). Among these samples, the pores of ASC-700 show a dense and homogeneous distribution, which improves its ionic storage and transport ability.

GCD tests were used to investigate the electrochemical capacitive performances of all the ASC samples (Fig. 4 and Fig. S6, ESI†). The GCD curves obtained in $H_2SO_4$ solution exhibit typical symmetric triangular shapes between −0.8 and 0.2 V *versus* $Hg/Hg_2SO_4$ (Fig. 4A) with no obvious ohmic drop, indicating the low internal resistance and good coulombic efficiency.[5] And the specific capacitance of the optimal material reaches 401 F $g^{-1}$ at 1.0 A $g^{-1}$ as calculated through eqn (1). Such a result is much higher than the previously reported data of other biomass based carbon materials (Table S3, ESI†), such as lotus stems, auricularia, moringa oleifera and honey derived carbons under similar test conditions (three-electrode systems with aqueous electrolytes).[12,28–41] The specific capacitance (ASC-700) decreases gradually with increasing current density, and retains 275 F $g^{-1}$ even at 30 A $g^{-1}$, indicating an excellent rate capability. In contrast, although ASC-600 has higher heteroatom contents, its surface area and pore volume are much lower than those of ASC-700 and ASC-800. Besides, a lower carbonization temperature means a lower graphitization degree, resulting in a higher internal resistance of the ASC-600 (Fig. S8, ESI† semicircles at high frequency refer to charge transfer resistance).[5,42] Hence, ASC-600 shows a lower capacitance (Fig. S9, ESI†). As for ASC-800, although it has a high graphitization degree, its mesopores are significantly few (Table 1), which cannot provide enough channels for ion transportation from the solution to the microporous surface. In addition, the Nyquist plot at the low frequency region is a vertical line for an ideal electrode material, and the more vertical the line, the better the capacitive performance it shows.[5,42] In comparison with the results of different samples (Fig. S8, ESI†), the slopes of ASC-700 and ASC-800 are much higher than those of ASC-600 and SC-700. Therefore, ASC-700 show better capacitive properties among all the samples. Its large specific surface area provides a huge adsorbing platform for charge accumulation, its appropriate number of mesopores interconnected with micropores supplies channels for ion transportation, and its rich surface functional groups offers Faraday reactions for pseudocapacitance. As the optimal example, ASC-700 has a capacity retention rate of 88.1% at 1 A $g^{-1}$, 90.3% at 2 A $g^{-1}$, and 94.5% at 5 A $g^{-1}$, respectively, after 10 000 cycles. Both ASC-600 and ASC-800 samples also show excellent cycling stabilities (Fig. 4B and Fig. S9, ESI†).

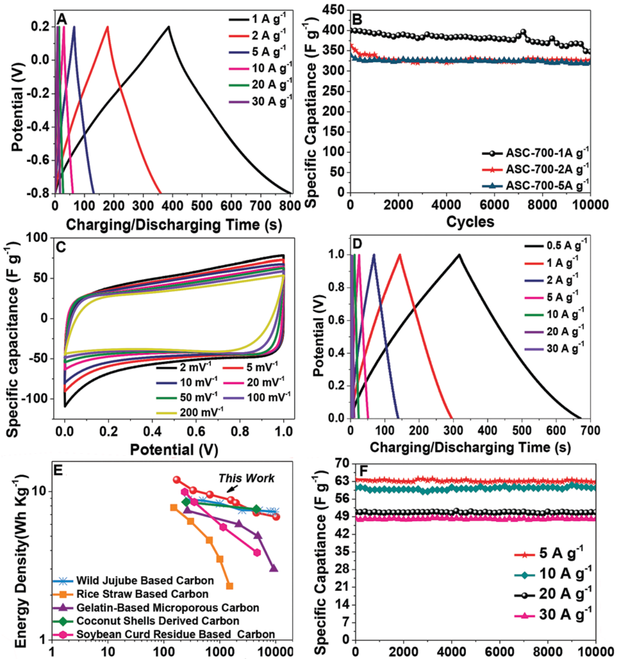

Fig. 4 Three-electrode system: (A) GCD curves and (B) cycling stability of ASC-700 at various current densities. Two-electrode system: (C) CV curves of the symmetric EDLCs based ASC-700 at a scan rates of 2–100 mV $s^{-1}$, (D) GCD curves of the symmetric EDLCs based ASC-700 at current densities of 1–30 A $g^{-1}$, (E) Ragone plots of the device of this study and porous carbon based aqueous symmetric EDLCs reported previously[27,32,37–39] and (F) cycle stability of the symmetric EDLCs based ASC-700 at various current densities.

Symmetric EDLCs are assembled by using ASC-700 as the positive electrode/negative electrode. No obvious peaks of the CV curves (Fig. 4C) are evident and the shapes of the curves are almost square, revealing characteristic capacitor behavior. Meanwhile, the voltage curves (Fig. 4D) demonstrate a slight deviation from the linear slope of ideal EDLCs, suggesting the same characteristics. The maximum specific capacitance (CM) based on the total mass of the active materials of the two electrodes is 86.5 F $g^{-1}$ at a current density of 0.5 A $g^{-1}$ (eqn (2)), which marks a striking increase in comparison with the previously reported porous carbon (obtained from complex methods or valuable precursors).[43–45] In addition, the power density and energy density are key indicators of the energy-storage performance and their feasibility for the relevant applications. According to eqn (3) and (4), such symmetric EDLCs deliver an energy density of 12.01 W h $kg^{-1}$ at a power density of 165 W $kg^{-1}$, and an energy density of 6.8 W h $kg^{-1}$ at a super high power density of 10 200 W $kg^{-1}$ (Fig. 4E). These results outperform a great number of existing biomass-based carbons, such as jujube-based carbon (8.8 W h $kg^{-1}$),[29] rice straw carbon (7.8 W h $kg^{-1}$),[34] gelatin-based microporous carbon (7.43 W h $kg^{-1}$)[45] and other aqueous symmetric EDLCs under similar conditions (two-electrode systems with aqueous electrolytes).[36–41,43–49] It should be noted that a two-step preparation is desired, namely pre-carbonization and low temperature activation, to yield the above-named biomass-based carbon materials, which is ascribed to the involvement of corrosive activation agents (*e.g.* KOH). As a result, this increases the production cost to a certain degree. The life-span of materials is also crucial to the EDLCs devices in practical applications. The cycling stability of our proposed materials and devices remains around 100% of its original value even measured at various current densities (Fig. 4F), indicating an encouraging future for commercialization.

Thus the selection of the biomass precursor and activation agent are key for high-performance carbon electrode materials. More specifically, the pseudocapacitance arises from a series of nitrogen/oxygen containing groups, which can be ascribed to SC with rich organics.[49] Moreover, the as-prepared 3D cross-linked carbon skeleton and the porous structures obtained from a mild process prove that $K_2C_2O_4$ is a good activation agent. After activation, carbon with a large specific surface area and meso–micro porous structure will provide a vast adsorbing platform for charge accumulation and fast transmission.[50–53] The combination of these two facilitates the formation of carbon materials with a high surface area (more than 1000 $m^2\ g^{-1}$), hierarchical pores (micro-meso pores), surficial groups (nitrogen/oxygen containing groups), and consequently high-performance EDLCs.

## Conclusions

This work develops a simple one-step preparation method for a series of hierarchical porous carbon materials involving SC as the precursor and $K_2C_2O_4$ as a mild activation agent. These biomass-derived carbon materials display a high surface area, the appropriate PSDs, cross-link networks, and high nitrogen/oxygen contents. The optimal material (ASC-700) exhibits striking electrochemical performance, including a capacitance of up to 401 F $g^{-1}$ at 1 A $g^{-1}$ and a capacitance retention of 94.5% at 5 A $g^{-1}$ over 10 000 cycles in 1 M $H_2SO_4$ aqueous electrolyte. The symmetric EDLCs also perform remarkably in terms of energy storage. Such an outstanding performance is ascribed to three main advantages of the proposed carbon materials. Firstly, hierarchical pore distribution and large SSA (1123.8 $m^2\ g^{-1}$) provide sufficient space for the storage of ions, short cuts for ion transport and thus contribute greatly to the electric double-layer capacitance. Furthermore, nitrogen and oxygen heteroatoms from the components of SC are able to induce faradaic reactions, enhance the surface compatibility with aqueous electrolytes, and provide low resistance pathways for ions. Finally, mild activation-carbonization processes endow the carbon materials' 3D solid skeletons, which exhibit excellent charging–discharging repeatability. Therefore, our present porous carbon materials have potential applications in electrochemical storage devices such as EDLCs and the Li-ion battery.

## Conflicts of interest

There are no conflicts to declare.

## Acknowledgements

This work was supported by the National Natural Science Foundation of China (21471047, 21271048, 21271045 and 21771039), the National Major Basic Research Program of China (2013CB934101), the Shanghai Science and Technology Committee (16DZ2270100), the Research Project of the Chinese Ministry of Education (213023A), the Excellent Youth Foundation of Henan Scientific Committee (124100510004), and the Program for Innovative Research Team in the University of Henan Province (14IRTSTHN005).

## Notes and references

1 X. Zhang, J. Luo, W. Lv, D. W. Wang and Q.-H. Yang, *Adv. Mater.*, 2015, **27**, 5388–5395.

2 J.-S. Wei, H. Ding, P. Zhang, Y.-F. Song, J. Chen, Y.-G. Wang and H.-M. Xiong, *Small*, 2016, **12**, 5927–5934.

3 Y. Zhu, X. Ji, C. Pan, Q. Sun, W. Song, L. Fang, Q. Chen and C. E. Banks, *Energy Environ. Sci.*, 2013, **6**, 3665–3675.

4 Y. Xu, Y. Tao, X. Zheng, H. Ma, J. Luo, F. Kang and Q.-H. Yang, *Adv. Mater.*, 2015, **27**, 8082–8087.

5 J.-S. Wei, H. Ding, Y.-G. Wang and H.-M. Xiong, *ACS Appl. Mater. Interfaces*, 2015, **7**, 5811–5819.

6 Y. Zhu, S. Murali, M. D. Stoller, K. J. Ganesh, W. Cai, P. J. Ferreira, A. Pirkle, R. M. Wallace, K. A. Cychosz, M. Thommes, D. Su, E. A. Stach and R. S. Ruoff, *Science*, 2011, **332**, 1537–1541.

7 D.-D. Zhou, W.-Y. Li, X.-L. Dong, Y.-G. Wang, C.-X. Wang and Y.-Y. Xia, *J. Mater. Chem. A*, 2013, **1**, 8488–8496.

8 B. Li, F. Dai, Q. Xiao, L. Yang, J. Shen, C. Zhang and M. Cai, *Adv. Energy Mater.*, 2016, **6**, 1600802.

9 Y. Zhai, Y. Dou, D. Zhao, P. F. Fulvio, R. T. Mayes and S. Dai, *Adv. Mater.*, 2011, **23**, 4828–4850.

10 X. Wei, Y. Li and S. Gao, *J. Mater. Chem. A*, 2017, **5**, 181–188.

11 Z. Guo, D. Zhou, H. Liu, X. Dong, S. Yuan, A. Yu, Y. Wang and Y. Xia, *J. Power Sources*, 2015, **276**, 181–188.

12 Y. Zhang, S. Liu, X. Zheng, X. Wang, Y. Xu, H. Tang, F. Kang, Q.-H. Yang and J. Luo, *Adv. Funct. Mater.*, 2017, **27**, 1604687.

13 N. M. Osman, I. A. Mohamed Ahmed and E. E. Babiker, *Int. J. Food Sci. Technol.*, 2009, **45**, 124–132.

14 W. D. Zhang, Y. Wang, Q. Wang, W. J. Yang, Y. Gu, R. Wang, X. M. Song and X. J. Wang, *J. Sep. Sci.*, 2012, **35**, 2054–2062.

15 Y.-D. Chen, W.-Q. Chen, B. Huang and M.-J. Huang, *Chem. Eng. Res. Des.*, 2013, **91**, 1783–1789.

16 L. Qie, W. Chen, H. Xu, X. Xiong, Y. Jiang, F. Zou, X. Hu, Y. Xin, Z. Zhang and Y. Huang, *Energy Environ. Sci.*, 2013, **6**, 2497–2504.

17 S. Gao, Y. Chen, H. Fan, X. Wei, C. Hu, H. Luo and L. Qu, *J. Mater. Chem. A*, 2014, **2**, 3317.

18 Z. Li, Z. Xu, X. Tan, H. Wang, C. M. B. Holt, T. Stephenson, B. C. Olsen and D. Mitlin, *Energy Environ. Sci.*, 2013, **6**, 871.

19 N. Gavrilov, I. A. Pašti, M. Vujković, J. Travas-Sejdic, G. Ćirić-Marjanović and S. V. Mentus, *Carbon*, 2012, **50**, 3915–3927.

20 D. Hulicova-Jurcakova, M. Seredych, G. Q. Lu and T. J. Bandosz, *Adv. Funct. Mater.*, 2009, **19**, 438–447.

21 X. Xiang, E. Liu, Z. Huang, H. Shen, Y. Tian, C. Xiao, J. Yang and Z. Mao, *J. Solid State Electrochem.*, 2010, **15**, 2667–2674.

22 S. Wu, X. Wu, G. Wang, L. Li, K. Tang, K. Huang, S. Feng, X. Dong, Z. Liu and B. Zhao, *Electrochim. Acta*, 2016, **218**, 66–73.

23 M. Sevilla, G. A. Ferrero and A. B. Fuertes, *Carbon*, 2017, **114**, 50–58.

24 X. Wei, H. Zou and S. Gao, *Carbon*, 2017, **123**, 471–480.

25 X. Wei, S. Wan and S. Gao, *Nano Energy*, 2016, **28**, 206–215.

26 J. Hayashia, T. Horikawa, I. Takeda, K. Muroyama and F. N. Ani, *Carbon*, 2002, **40**, 2381–2386.

27 X. He, P. Ling, M. Yu, X. Wang, X. Zhang and M. Zheng, *Electrochim. Acta*, 2013, **105**, 635–641.

28 B. Liu, Y. Liu, H. Chen, M. Yang and H. Li, *J. Power Sources*, 2017, **341**, 309–317.

29 K. Sun, S. Yu, Z. Hu, Z. Li, G. Lei, Q. Xiao and Y. Ding, *Electrochim. Acta*, 2017, **231**, 417–428.

30 C. Long, X. Chen, L. Jiang, L. Zhi and Z. Fan, *Nano Energy*, 2015, **12**, 141–151.

31 H. Feng, H. Hu, H. Dong, Y. Xiao, Y. Cai, B. Lei, Y. Liu and M. Zheng, *J. Power Sources*, 2016, **302**, 164–173.

32 L. Chen, T. Ji, L. Mu and J. Zhu, *Carbon*, 2017, **111**, 839–848.

33 N. Sudhan, K. Subramani, M. Karnan, N. Ilayaraja and M. Sathish, *Energy Fuels*, 2017, **31**, 977–985.

34 A. K. Mondal, K. Kretschmer, Y. Zhao, H. Liu, C. Wang, B. Sun and G. Wang, *Chem. – Eur. J.*, 2017, **23**, 3683–3690.

35 Y. Cai, Y. Luo, Y. Xiao, X. Zhao, Y. Liang, H. Hu, H. Dong, L. Sun, Y. Liu and M. Zheng, *ACS Appl. Mater. Interfaces*, 2016, **8**, 33060–33071.

36 J. Li, G. Zan and Q. Wu, *New J. Chem.*, 2015, **39**, 8165–8171.

37 C. Wang and T. Liu, *J. Alloys Compd.*, 2017, **696**, 42–50.

38 Z. Sun, J. Liao, B. Sun, M. He, X. Pan, J. Zhu, C. Shi and Y. Jiang, *Int. J. Electrochem. Sci.*, 2017, **12**, 12084–12097.

39 S. Zhang, K. Tian, B.-H. Cheng and H. Jiang, *ACS Sustainable Chem. Eng.*, 2017, **5**, 6682–6691.

40 J. Hao, Y. Huang, C. He, W. Xu, L. Yuan, D. Shu, X. Song and T. Meng, *Sci. Rep.*, 2018, **8**, 562.

41 J. Yi, Y. Qing, C. Wu, Y. Zeng, Y. Wu, X. Lu and Y. Tong, *J. Power Sources*, 2017, **351**, 130–137.

42 C. Yang, C.-Y. V. Li, F. Li and K.-Y. Chan, *J. Electrochem. Soc.*, 2013, **160**, H271–H278.

43 X.-Y. Chen, C. Chen, Z.-J. Zhang and D.-H. Xie, *Ind. Eng. Chem. Res.*, 2013, **52**, 12025–12031.

44 Y. An, Y. Yang, Z. Hu, B. Guo, X. Wang, X. Yang, Q. Zhang and H. Wu, *J. Power Sources*, 2016, **337**, 45–53.

45 G. Chen, S. Wu, L. Hui, Y. Zhao, J. Ye, Z. Tan, W. Zeng, Z. Tao, L. Yang and Y. Zhu, *Sci. Rep.*, 2016, **6**, 19028–19037.

46 H. Fan and W. Shen, *ACS Sustainable Chem. Eng.*, 2016, **4**, 1328–1337.

47 A. Jain, C. Xu, S. Jayaraman, R. Balasubramanian, J. Y. Lee and M. P. Srinivasan, *Microporous Mesoporous Mater.*, 2015, **218**, 55–61.

48 G. Ma, F. Ran, H. Peng, K. Sun, Z. Zhang, Q. Yang and Z. Lei, *RSC Adv.*, 2015, **5**, 83129–83138.

49 J. Wang, L. Shen, Y. Xu, H. Dou and X. Zhang, *New J. Chem.*, 2015, **39**, 9497–9503.

50 M.-X. Liu, L.-Y. Chen, D.-Z. Zhang, H. Duan, W. Xiong, Z.-J. Xu, L.-H. Gan and L.-W. Chen, *Chin. Chem. Lett.*, 2016, **27**, 299–404.

51 L. Miao, D. Zhu, Y. Zhao, M. Liu, H. Duan, W. Xiong, Q. Zhu, L. Li, Y. Lv and L. Gan, *Microporous Mesoporous Mater.*, 2017, **253**, 1–9.

52 X. Ma, M. Liu, L. Gan, Y. Zhao and L. Chen, *J. Solid State Electrochem.*, 2013, **17**, 2293–2301.

53 D. Zhu, Y. Wang, W. Lu, H. Zhang, Z. Song, D. Luo, L. Gan, M. Liu and D. Sun, *Carbon*, 2017, **111**, 667–674.